

# Decomposing rhythmic hippocampal data to obtain neuronal correlates

J.A. Gillis<sup>a,b,\*</sup>, W.P. Luk<sup>a,d,1</sup>, L. Zhang<sup>a,c,d,1</sup>, F.K. Skinner<sup>a,b,c,e,2</sup>

<sup>a</sup> The Toronto Western Research Institute, UHN, Toronto, Ont., Canada M5T 2S8

<sup>b</sup> Department of Physiology, University of Toronto, Toronto, Ont., Canada M5S 1A8

<sup>c</sup> Faculty of Medicine (Neurology), University of Toronto, Toronto, Ont., Canada M5B 1W8

<sup>d</sup> Institute of Medical Science, University of Toronto, Toronto, Ont., Canada M5S 1A8

<sup>e</sup> IBBME, University of Toronto, Toronto, Ont., Canada M5S 3G9

Received 28 May 2004; received in revised form 3 February 2005; accepted 25 March 2005

---

## Abstract

Characterizing hippocampal electrical rhythmic activities requires a broadly applicable methodology that lends itself to physiological interpretation. In the intact hippocampal preparation, spontaneous rhythmic field potentials are exhibited in the 3–4 Hz range which evidence suggests is due to discharges in the inhibitory interneuron population. Because field rhythms arise as a network effect and models must be built from the neuron up, we focus on developing a methodology to deconstruct the non-stationary rhythms into its important constituents. This study uses 50 CA1/CA3 local field potentials to determine the important constituents, and an additional field recording and two intracellular recordings are examined subsequently. We determine the suitability of several time–frequency techniques. Distinct regions in the time–frequency domain which account for the signal behaviour are then characterized in terms of duration and frequency. These characteristics are interpreted as arising from a statistical mixture distribution. The decomposition of the 50 recordings yields three components whose patterns of activity match those of the intracellular recordings. We suggest that the statistical variability of the local field data can be linked to the variability of neuronal activities seen in intracellular data.

© 2005 Elsevier B.V. All rights reserved.

**Keywords:** Time–frequency; EEG; Cluster; Intracellular; Deconstruction; Mixture distributions; Oscillations

---

## 1. Introduction

Several brain structures including the hippocampus exhibit a diversity of rhythmic oscillations, often considered primarily in terms of frequency. The role of rhythms is frequently elucidated through correlative means (e.g., Sirota et al., 2003) with a focus on specific characteristics, and partic-

ularly frequencies. Extracellular and electroencephalogram (EEG) recordings of the hippocampus reveal the presence of rhythmic activities associated with distinct behavioural states. Coherent network rhythmic activity occurs in three main clusters in freely moving rodents: large amplitude irregular activity (LIA, 0.5–20 Hz), rhythmic slow activity (RSA, 4–10 Hz), and fast oscillatory activity (30–100 Hz) (Csicsvari et al., 2000; Vanderwolf, 1969). Although the role of these rhythms is not yet perspicuous, they have been functionally implicated in synaptic plasticity (Huerta and Lisman, 1993), sensory-motor behaviour (Oddie and Bland, 1998), and learning and memory processing (Kudrimoti et al., 1999).

These rhythms arise from networks of interconnected cells. Electrophysiological features of the specific cells are important and will depend on the particular brain structure involved. The general problem of completely characterizing hippocampal rhythms can be subdivided into spatial and temporal avenues of research, and their combination. On the spa-

---

\* Corresponding author at: Division of Cellular and Molecular Biology, The Toronto Western Research Institute, Main Pavilion, Room MP13-308, 399 Bathurst Street, Toronto, Ont., Canada M5T 2S8.  
Tel.: +1 416 603 5800x5066; fax: +1 416 603 5745.

E-mail address: jesse.gillis@utoronto.ca (J.A. Gillis).

<sup>1</sup> Division of Cellular and Molecular Biology, The Toronto Western Research Institute, Main Pavilion, Room MP13-411, 399 Bathurst Street, Toronto, Ont., Canada M5T 2S8.

<sup>2</sup> Division of Cellular and Molecular Biology, The Toronto Western Research Institute, Main Pavilion, Room MP13-317, 399 Bathurst Street, Toronto, Ont., Canada M5T 2S8.

tial side, recordings from multiple cells simultaneously offer an avenue to examine the variability in the cell and network rhythm within the hippocampus. In particular, multielectrode recordings allow an examination of the cellular variability that gives rise to network behaviour by recording from the individual cells in a rhythmic network (Nicolelis and Ribeiro, 2002). On the frequency side, at present, filtering and spectral analyses are used to characterize rhythmic data. The suitability of such techniques are data dependent, and particularly upon the degree to which the signal changes in time; that is, its non-stationarity. This is a well-known problem and specialized techniques have been developed for particular data sets (e.g., Achermann and Borbély, 1998). Developing data specific methodologies presents its own difficulties in terms of hypothesis and verifiability. A methodology developed specifically to suit the data may be unfalsifiable (e.g. overfitting), while a methodology not specifically developed to be suitable to the data can be biasing if, for example, a chosen filter is inappropriate. Ideally, a methodology is both testable and unbiased, or, at least, testable in its biases. We attempt to satisfy this balance by taking a very broad look at neuronal population rhythms, developing an interpretation testable against physiology, and then comparing with intracellular data. Recently, the investigation of the frequency of neuronal firing has been expanded and broadened to include spike correlations and more complex elements of the pattern in time and frequency (e.g., Gray et al., 1989; Nicolelis et al., 1995; Rieke et al., 1997). Specifically, using time–frequency techniques allows the examination of the variability of rhythm in the temporal domain—signals with changing frequency distributions are known as non-stationary in this context. Further, because hippocampal rhythms are often examined in a correlative way, it is useful to obtain a characterization that is not dependent on external factors—finding a natural, *a priori*, characterization which can later be examined for independent patterns.

In this paper, we focus on the variation of the population rhythms seen in extracellular recordings in the time–frequency domain. We develop a method which allows us to reduce a population rhythm to basic characteristics and we apply the methodology to the experimental data of Wu et al. (2002). The aim of this paper is to use accepted techniques in a novel combination and thereby present a method which may be used to characterize hippocampal rhythms in a way that can be physiologically interpreted. More specifically, we hope to leave the methodology general enough to provide for broad applicability in deconstructing field potential rhythms and relating them to the activity of components, down to the level of neurons.

The method uses standard techniques of time–frequency ( $T$ – $F$ ) analyses, object identification and mixture distributions.  $T$ – $F$  analysis is a technique for determining the frequency behaviour of a signal over time (e.g., Adeli et al., 2003); object identification uses the characteristics of a surface, often gradient or amplitude, to determine boundaries for regions in the surface (e.g., Ponomarev and Davis, 2003), typ-

ically on a surface; mixture distributions can be regarded as close to a form of cluster analysis and allows the probabilistic separation of data that arises from overlapping statistical distributions (e.g., Everitt and Bullmore, 1999). While these individual techniques have been used in neuroscience and biology previously, they have not been used together in this fashion before and constitute a novel methodology applied to rhythmic experimental data. We use  $T$ – $F$  analysis as a natural framework to analyze a varying rhythm and then determine strongly contributory regions of the signal (in the  $T$ – $F$  domain) using object identification, and analyze the properties of these signal characteristics using mixture distributions.

## 2. Methods

### 2.1. Data collection and processing

Structurally, the hippocampus is organized in layers so that connectivity occurs within a plane defined by the cell bodies (Johnston and Amaral, 1998), making it particularly well suited to analysis in slice. Hippocampal slice preparations have been a useful *in vitro* model system for the purpose of determining the cellular genesis of these rhythms. The slice preparation offers the convenience of single cell recordings and pharmacological manipulations but it contains only limited network connectivity. Functionally significant long-range neuronal hippocampal connections (Andersen et al., 2000; Li et al., 1994) and function (Hampson et al., 1999; Moser and Moser, 1998) are disrupted during the slicing procedure.

The disruption imposed by the slice model has recently been addressed by Wu et al. (2002) in their development of a novel *in vitro* mouse hippocampal preparation. Their approach is to isolate the whole hippocampus from 21- to 28-day-old mice and remove the dentate gyrus while maintaining CA3–CA1 connectivities. While perfusing the hippocampal isolate *in vitro* at 32 °C, Wu et al. observed 0.5–4.0 Hz spontaneous rhythmic field potentials (SRFPs) in their extracellular recordings. Their data suggest that the SRFPs represent the summation of inhibitory post-synaptic potentials arising from the pyramidal neuron population as the result of synchronous discharges of inhibitory interneurons. Because intracellular stimulation of individual interneurons did not alter local SRFPs, Wu et al. suggested an important role for the networking of interneurons in providing a basis for the rhythm observed. However, such interpretations are limited to the degree of precision to which the signal itself is characterized.

In this paper, we examined the SRFPs and associated rhythmic activities recorded from the mouse hippocampal isolate. The experimental methods have been described previously (Wu et al., 2002). Briefly, C57bl mice of 21–28 days old (Charles River, Que., Canada) were decapitated under halothane anaesthesia. The brain was dissected out, hemi-sectioned and placed in an ice-cold artificial cerebrospinal fluid (ACSFs) for several minutes before further dissection.

The hemi-sectioned brain was dissected to obtain the hippocampus and the dentate gyrus beyond the hippocampal fissure was removed. The resulting tissue section was roughly flat and approximately 0.6 mm thick, including CA1, CA2, and CA3b regions. The dissected hippocampal isolate was kept in oxygenated ACSF for at least 1 h before recording. The components of the ACSF were (in mM): 3.5 KCl, 1.25  $\text{NaH}_2\text{PO}_4$ , 125 NaCl, 25  $\text{NaHCO}_3$ , 2  $\text{CaCl}_2$ , 1.3  $\text{MgSO}_4$  and 10 Glucose. The pH of ACSF was  $\sim 7.4$  when aerated with 95%  $\text{O}_2$ –5%  $\text{CO}_2$ .

Extracellular recordings were made from the hippocampal isolate in the CA1/CA3 region in a submerged recording chamber at 32 °C. Extracellular recording electrodes were pulled from thin-wall glass pipettes (OD 1.5 mm, World Precision Instruments, Sarasota, Florida, USA). The resistance of these electrodes was  $\sim 2 \text{ M}\Omega$  after being filled with the solution containing 200 mM NaCl and 2 mM HEPS (pH 7.4). Extracellular field potentials were sampled through an Axoclamp-2A amplifier (Axon Instruments, Foster City, CA), and the signals were further amplified to a total gain of 10 000x before digitization (Digidata 1200, Axon Instruments Inc., Union City, CA, USA). The frequency band of the Axoclamp-2A amplifier was set in the range of dc–1 KHz, and the digitization rate was approximately 20 000 Hz.

Electrodes for whole-cell patch recordings were pulled from the similar thin wall glass tube described above, and their resistances were  $\sim 5 \text{ M}\Omega$  after being filled with the solution that contained 150 mM potassium gluconate, 2 mM HEPES and 0.1 mM EGTA. The pH of patch pipette solutions was adjusted to 7.25 with KOH and osmolarity was 280–290 mOsm. Whole cell recordings were conducted via using the Axoclamp-2A or a Axopatch 200B amplifier. Data acquisition, storage and initial analyses were done using pCLAMP software (version 8 or 9, Axon Instruments).

Fifty extracellular recording sets, each being approximately 3 min in duration, were used in the present analyses. We also examined some intracellular data collected from CA1 pyramidal neurons and an additional extracellular data set. Data analysis was performed using Matlab and Matlab packages.

## 2.2. Power spectra analysis

The power spectra of each of the recordings was examined, and the distribution of activity characterized according to its range, means, artifacts, and pattern of activity (e.g., distribution shape).

Using 5–10 recording sets, the stationarity of the signal was examined over a range of intervals from 0.05 to 5 s visually and by calculating variation in the spectra with respect to mean and variance (see Appendix A). In particular, the suitability of the signal for windowing at 0.05, 0.1, 0.2, 0.4, 0.8, 1, 2, 3, 4 and 5 s was examined for 20 randomly selected intervals within each signal recording intended for analysis. Different window types (Kaiser, Gaussian, Hamming, rectangular) were examined for their effects.

## 2.3. Time–frequency (T–F) analysis

Three time–frequency transforms drawn from Cohen’s class and one wavelet transform were used in the analysis. The first of Cohen’s class of distribution used was the Gaussian windowed short-time Fourier transform (STFT), also known as the Gabor transform (see Appendix A). A discrete form of the STFT is given by:

$$\text{STFT}(k, n) = \sum_{m=0}^{L-1} x(n+m)g(m) \exp\left(\frac{-2i\pi mk}{N}\right) \quad (1)$$

where  $k$  is the frequency,  $n$  the time going up to  $N$ ,  $L$  the discrete window length, and  $g(m)$  is a Gaussian window:

$$g(m) = \exp\left[-\left(2 - \frac{4m}{L-1}\right)^2\right], \quad 0 \leq m \leq L-1 \quad (2)$$

The Gaussian window,  $L$ , was chosen on the basis of the stationarity properties with width corresponding to 0.1, 0.2, 0.25, 0.3, 0.5, 1, 2, 3, 4, and 5 s. That is, time–frequency methods assume stationarity within a signal segment, and so window choice must be appropriate to the rate at which the signal behaviour changes and depending on the features of interest (Tomazic, 1996). The behaviour exhibited by the frequency distribution over time was also examined with relation to correlations present at different times, and the pattern of non-stationarity.

The second of Cohen’s class was the Wigner distribution (Wigner, 1932; see Appendix A). No smoothing was used and particular attention was paid to possible areas of interference between components. In particular, the STFT was used as a baseline to determine the extent of multi-component interference. The discrete Wigner distribution was determined by taking the discrete-time Fourier transform of the local autocorrelations with parameters defined as in the STFT, and with linear interpolation between values. Smoothing of the resultant time–frequency distributions was performed using Gaussian smoothing only after an examination of the interference present. The other two transforms (Choi–Williams and the Haar wavelet transform) are described in Appendix A.

Cross-term interference is a general property of bilinear time–frequency representations where different subcomponents interact (cross-terms), allowing a time–frequency representation to be non-zero even if the signal is zero (Kadambe and Boudreaux-Bartels, 1992). This is discussed further in Appendix A. Generally speaking, just as there is a tradeoff between time resolution and frequency resolution (the Uncertainty principle), there is a tradeoff between the joint resolution and the degree of interference. The spectrogram (produced by the STFT) has virtually none, while the Wigner is sometimes considered unusable due to the cross-terms and we examined these two extremes. The intermediate case of the Choi–Williams, and a specific wavelet transform were also considered (see Appendix A) to cover a reasonable range of properties for developing our methodology.

## 2.4. Object identification and characterization

Local areas in the time–frequency domain of the STFT with distinct power were identified, henceforth called “objects” in the time–frequency domain. This was accomplished according to two criteria:

- (1) High power to determine regions in which objects may lie.
- (2) The presence of a distinct edge surrounding the peak within a region to determine the object perimeter.

Because we are concerned with detecting qualitatively visible and quantitatively important areas in the signal, high power is a useful criterion to use (Morrone and Owens, 1987). For our first criterion, we used a simple cutoff based on the number of separate regions rising above the high power threshold. The number of time–frequency domains rising above a given power was plotted as a function of power (Fig. 4A). Note that this does not constitute object identification; it is only the first step. The natural cutoff power was defined as being the one with the maximum number of distinct regions above that cutoff power; that is, the power when the number of new regions appearing was balanced by the merging together of previously distinct regions. This can be thought of as balancing competing requirements to be exhaustive and non-overlapping.

The edge for objects in the time–frequency domain was determined using a Laplacian technique (Marr and Hildreth, 1980). In this sense, and consistent with ordinary experience, an edge occurs when the gradient is relatively high in magnitude (see Appendix A). Applying this criterion reduces the number of objects detected from the number of regions identified using the natural cutoff power—some high power regions would not have a well-defined perimeter around a peak. Time–frequency data was interpolated onto a fixed higher resolution grid ( $0.1 \text{ Hz} \times 0.1 \text{ s}$ ) using cubic splines (in both directions); this high resolution (relative to the uncertainty relation) will have an effect because the interpolation is not linear, effectively allowing a weighting to characterize edges with greater resolution. Zeros in the Laplacian were then used to define the edge of the time–frequency objects. Note that this is similar to using the Mexican Hat wavelet at a particular scale. If the perimeter went outside of the identified region, the object was excluded as being insufficiently local. The edge detection applied was scaled to be appropriate to the resolution of the time–frequency domain; that is, additional smoothing was not applied.

The path of the perimeter was then limited to points that would leave rays from the centre cutting the perimeter only once. This assumes a fairly simple shape for objects and will thus tend to exclude pieces of an object that visually would appear to have arisen due to the overlap of simpler shapes. The objects defined by these perimeters were characterized according to their mean frequency of operation and their duration of operation, even if that duration was less than the time of activity for any specific frequency. Note that the interpola-

tion and edge detection effectively performs a weighting by amplitude (relative to baseline) to obtain finer scale duration and frequency measures than the uncertainty relation strictly allows. That is, highs that are the result of very transient change will tend to be smaller. On the other hand, changes that occur too slowly will not generate an edge or be detected at all. This object identification protocol was also employed on randomly generated surfaces of smoothed noise.

## 2.5. Classifying time–frequency objects

The characteristic duration and frequency for the time–frequency objects, determined in our last step, were treated as observations arising from a statistical mixture of normal distributions. The expectation–maximization (EM) algorithm was used to determine the parameters for the statistical populations (Dempster et al., 1977).

A mixture distribution is a probability density function which can be written as a weighted sum of its constituent conditional probability functions. The weighting, or mixing coefficients, must sum to one, and the constituent distributions typically represent discrete classes of observation. In this paper we examined a bivariate mixture of normal distributions in the duration–frequency domain, with the goal of classifying the unknown data (probabilistically) into clusters. For  $k$  clusters, a mixture density  $f(y)$  has the form:

$$f(\vec{y}) = \sum_{j=1}^k p_j f_j(\vec{y}) \quad (3)$$

with  $p_j$  being the weighting coefficient and  $f_j$  representing the component density for the  $j$ th distribution with random variables  $y$ . In our case, we have bivariate data consisting of mean-frequency and duration values, and we are seeking to determine the  $f_j$  distributions which gave rise to that data. We used the entire pool of data from the 50 extracellular data sets to generate the distributions.

One technique to fit a distribution to the data generated by a presumed mixture is to use the EM algorithm (Dempster et al., 1977). The EM algorithm is a technique for dealing with incomplete data to determine the underlying distribution which generated it. As it operates, the EM algorithm will act to iteratively maximize the observed likelihood or log-likelihood data by an expectation step followed by a maximization step, and repeating. In the E step, the expectation of the log-likelihood for the particular case is determined conditionally from the observed data (given parameters used to determine the complete data in this step) and it is then substituted for the complete log-likelihood; In the M step the likelihood equations are solved to maximize the complete data log-likelihood (Everitt and Hand, 1981; Flury, 1997). In this case we are fitting a mixture of Gaussian distributions using the EM algorithm to determine the mean and covariance matrices which define them (see details in Appendix A).

The algorithm was terminated when the estimates for parameters differed by less than 0.1% after 100 iterations.



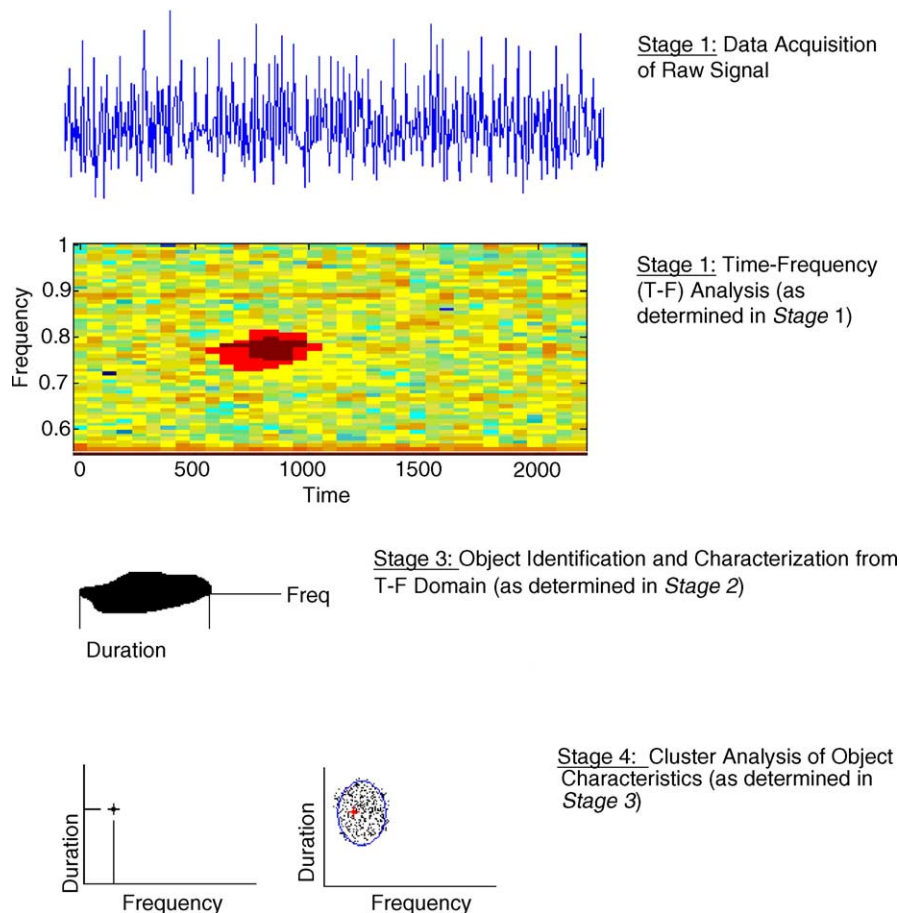


Fig. 1. A summary of the method. The four central stages in the method are shown via illustrations with arbitrary scale. Stage 1 is the data acquisition stage in which the raw signal is acquired from the experiments. The illustration here is of an artificial spiking signal. We used 50 sets of extracellular local field potential recordings from CA1/CA3 hippocampus which exhibited spontaneous rhythmic activity. Stage 2 is the time–frequency ( $T$ – $F$ ) analysis stage. The Gabor transform or short-time Fourier transform (STFT) is applied to each of the 50 data sets to produce 50  $T$ – $F$  plots or spectrograms. An illustration of a  $T$ – $F$  plot is shown in which a distinct high power region can be seen. In stage 3, objects are identified from each of the  $T$ – $F$  plots, and characterized in terms of frequency and duration. An example object is illustrated. About 10–50 objects were identified for each of the 50 data sets. Finally, in stage 4, a mixture distribution (cluster) analysis is applied to the identified object characteristics, as determined from all the  $T$ – $F$  plots, to produce distributions of best fit. Each point on the duration–frequency plot represents the characteristics of an object identified in stage 3. An illustration of one object's characteristics is shown on the left side of stage 4. The distribution overall would be determined from the object characteristics from all recordings (right side illustration of stage 4). See Section 2 for further details describing each of the stages.

Multiple values were used for starting estimates, and the variation in final estimates was taken as providing the error. A minimum of five different starting values were used for each parameter (i.e., means and variances of Gaussian distributions), with the values being equally interspersed in the ranges that were determined by those arising from the object detection. The number of statistical populations was determined both using a test of significance and by exhaustively adding distributions until estimates were no longer reasonable (e.g. accounting for outliers or noise, or too unstable). We used the likelihood ratio test statistic as an approximate test to determine our number of distributions (e.g., Wolfe, 1970), although it is known to deviate from a  $\chi^2$  distribution (McLachlan, 1987). That is, the number of statistical populations was increased until the difference between log-likelihood values for  $N$  clusters and  $N + 1$  clusters, proportional to the pseudo  $\chi^2$  value, became constant.

In Fig. 1, we summarize the entire method in four stages. Stage 1 illustrates an experimental signal that is acquired; stage 2, illustrates the time–frequency analysis of the signal; stage 3, the identification and characterization of objects from the  $T$ – $F$  domain; finally, stage 4, in which a mixture distribution of the object characteristics is generated.

### 3. Results

In previous work, Wu et al. (2002) obtained spontaneous rhythmic field potentials (SRFPs) in extracellular recordings from an intact whole hippocampal preparation in vitro. In that work, they conducted analysis primarily by visually counting peaks for sample durations to determine frequency, and sometimes using a filtered power spectra for the same purpose. Artifacts, such as the  $1/\text{frequency}$  dependence for low

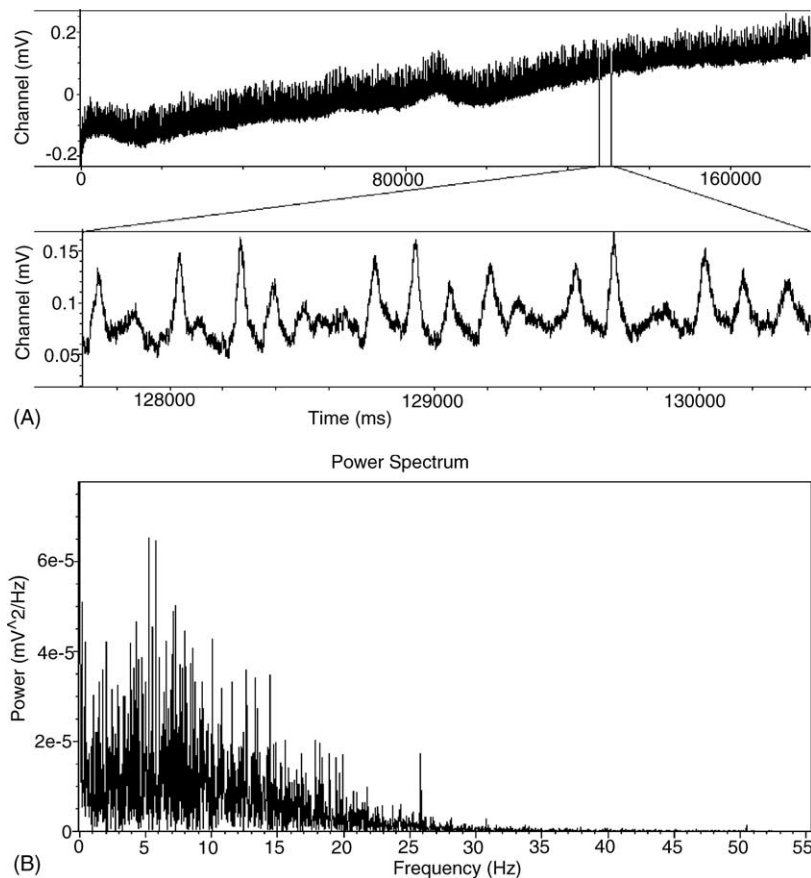


Fig. 2. Extracellular recording and its power spectrum. (A) An example of a 3 min extracellular local field recording from the intact hippocampus preparation, with an expanded view below showing a portion of the signal in detail. (B) The power spectrum of the entire 3 min signal in (A).

frequencies or changes in baseline, occurred throughout the data, but were distinct and generally separable from the frequency components representing hippocampal activity. Similarly, the artifact induced by electrical hum at 60 Hz (and its multiples) was clearly visible. An example extracellular recording is shown in Fig. 2A. The complex behaviour of the raw extracellular recording is reflected in the power spectrum which is shown in Fig. 2B. The range of frequencies present over the entire signal, which was quite broad, extended up to 25 Hz ( $\pm 7$  Hz) in the recordings to capture most (95%) of the signal energy.

We examined the power spectra for all 50 sets of recordings and found that the central distribution of frequencies had modes in a unimodal distribution of  $4.3 \pm 1.2$  Hz. Excluding the activity due to harmonics, the power spectra frequently exhibited multi-modality. The mean for distributions covered the full range of frequencies present but generally gave high errors using mixture distribution techniques; 20–30% with Gaussian fits and 10–40% with lognormal fits. As in Fig. 2B example, this seems likely to be due to the positive skew of the data when attempting to fit using normal distributions. The data also differed significantly ( $p < 0.01$ ) from both a normal and lognormal distribution. A 5 s window fast Fourier transform of signal data changed substan-

tially in distribution when shifted forward by its extent—we treated the mean and variance between epochs as the test for stationarity (Refinetti, 2004). Specifically, we took this to mean that the difference between the mean frequencies of consecutive windows was statistically significant using the Kruskal–Wallis test (at  $p < 0.05$ ), and also examined the variance of the frequency distributions—significant differences ceased at 0.25 s resolution. Looking outside the mean of the frequency distributions and at their specific form, there were very clear differences, including shifts from unimodality to multi-modality between a single set of consecutive windows.

Applying our method (as summarized in Fig. 1) to the 50 sets of extracellular recordings, we find that, taken altogether, the data fits to a mixture distribution with three components with specific parameters (Fig. 5), where both two and four components generated distributions with more significant anomalies with respect to the data. It is important to note that while these characteristics are identified in a specific framework (time–frequency domain), they encompass almost the entire signal domain (unlike, for example, filtering). We now describe details of applying our method to the field data in relation to the steps described in Section 2; that is, stages 2–4 as shown in Fig. 1.

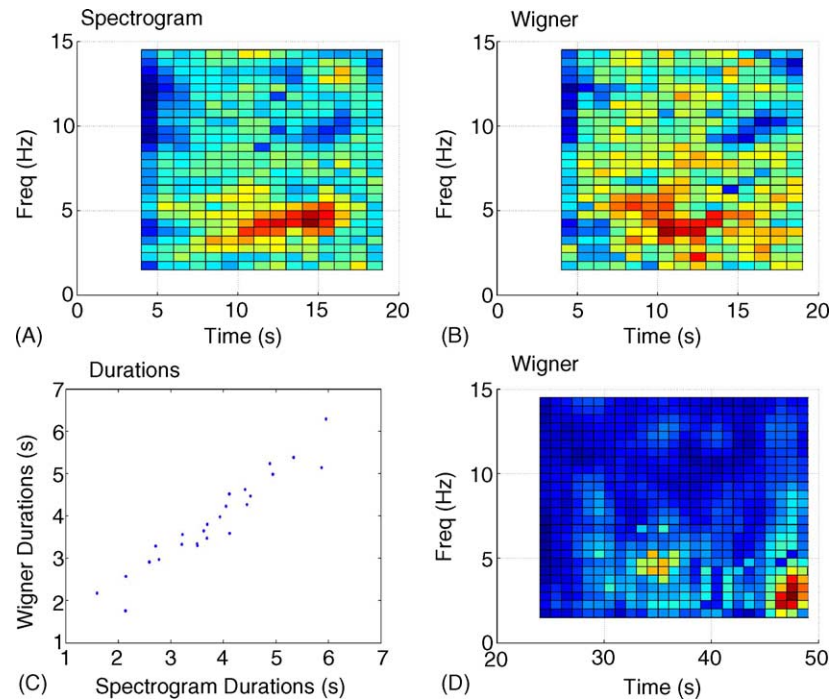


Fig. 3. Comparison between Wigner distribution and Spectrogram. (A) Spectrogram obtained from one of the hippocampal data sets. The time range of the  $T$ – $F$  plot shown is chosen so as to clearly illustrate a distinct region (seen in red) in the spectrogram. Note that this distinct region would give rise to an identified object if the power and perimeter criteria are met (see Section 2 for details). (B) Wigner distribution of the same data set used in (A) and shown at the same resolution as in (A). Similar qualitative features as in (A) can be seen but cross-term interference is also apparent. (C) Extracted object duration values obtained from  $T$ – $F$  plots of two 3 min data set using either the Wigner distribution or Spectrogram. (D) The Wigner distribution from another recording, at equivalent resolution to (A), (B) and (D) uses blues for low signal power (valleys) and reds for high signal power (peaks), with green and yellow representing intermediate powers.

### 3.1. Time–frequency analysis (stage 2)

Using the different time–frequency transforms described in Section 2, we find the following. The STFT or spectrogram showed a band of activity around the value of the main frequency component in the power spectra (approximately 4 Hz). This is illustrated in Fig. 3A which shows part of one data set. Within this band there were distinct peaks and valleys varying over time and frequency. Because the main band of activity was fairly narrow, harmonics were also clearly visible. Over the duration of the 3 min recording, the mean frequency frequently decreased or increased over the course of the recording—a shift on average of 1.2 Hz per recording, but trends towards increasing frequency were roughly as common as those towards decreasing frequency. The joint resolution appeared to be sufficient to examine features of the time–frequency domain within the dominant frequency band, using different window sizes where appropriate.

The time–frequency plots resulting from the Wigner distribution differed visibly from those of the STFT for the same signal but prominent features visible in one case were typically visible in the other when the same signal was analyzed (compare, for example, Fig. 3A and B). In particular, the same local time–frequency highs or objects were visible and at the same scale (Fig. 3C). Interference in the Wigner distribution, generating sharp spectral edges, was visible in the Wigner

distribution in areas where there was little signal activity. Treating the STFT for the same signal as our benchmark, the activity seen in the Wigner distribution shown in Fig. 3D in the 40–45 s range is an artifact of interference.

Different time–frequency representations will have properties useful under different conditions. In this case, none of the alternatives we explored showed substantial improvement over the STFT, which remains a standard choice. We did not find the Haar wavelet transform a particularly appropriate choice for our data, and the main advantage of wavelets (changing frequency resolution) is not helpful in this case. Thus, for our subsequent object identification and mixture distributions, the STFT was used.

### 3.2. Object identification and characterization (stage 3)

The STFT time–frequency plane exhibited symmetry in its generation of peaks and valleys above and below a threshold amplitude. This is illustrated in Fig. 4A for one data set. The edge detection within regions generated objects with distinct perimeters, as in the example shown in Fig. 4B. The number of objects detected per 3 min recording ranged from 10 to 50, with the total number in any signal comprising more than half of the power within their frequency range. The time evolution of object characteristics in a given recording (mean frequency, duration) was not entirely erratic—objects next

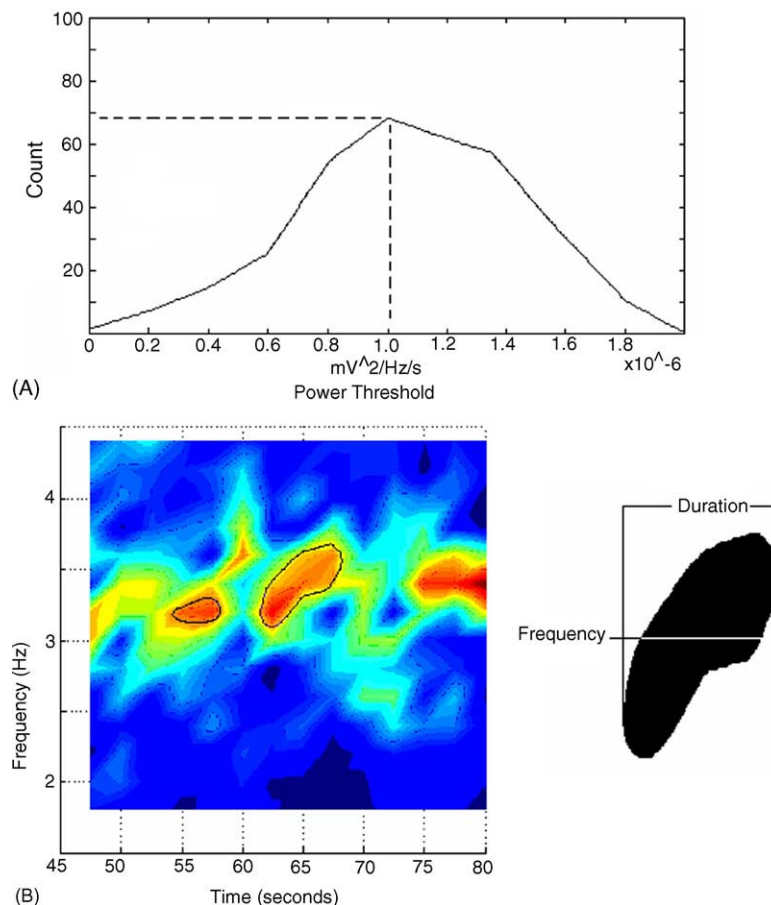


Fig. 4. Objects in the time–frequency ( $T$ – $F$ ) domain. (A) Plot of the number of distinct regions observed as cutoff threshold increases for one of the 50 data sets. Note that for this example, a threshold of about  $1 (\times 10^{-8} \text{ mV}^2/\text{Hz s})$  would be chosen by the method giving rise to about 70 distinct regions for this data set. (B) Left side shows the spectrogram of one of the data sets, illustrated in ranges to allow two distinct objects to be clearly visible in the  $T$ – $F$  plot. Identified objects (peak and perimeter criteria) are outlined in black. An illustration of a distinct shape, or single object characterized by frequency and duration, in the  $T$ – $F$  domain that the object detection algorithm finds is shown on the right side. Same color scheme as in Fig. 3.

to each other had more similar parameters than the average within a given recording. Any strong repetitive pattern in the presence of a few objects and their parameters might have suggested that a single feature was being misclassified, but this did not occur in any recording. The radial line criterion excluded fewer than 10% of points within an object in more than 95% of cases. That is, radial lines rarely cut the perimeter more than once, or cut off more than a minor outcropping, suggesting that few objects could be seen to be a merging of two simpler objects. The precise placement of adjacent objects in time–frequency exhibited no fixed relationship.

When applied to Gaussian smoothed noise, no objects were picked out for small-scale smoothing, and objects at the scale of the smoothing were picked out for large-scale smoothing. Although duration and mean frequency do not fully characterize objects detected in theory, in practice, shapes were sufficiently regular to make variation in terms of shape fairly small between objects sharing the same duration and mean frequency. Further, there was stability with respect to minor variation in the values for the natural power

threshold, degree of smoothing in the data, and nearness of the Laplacian to zero.

### 3.3. Feature classification (stage 4)

The number of objects obtained depends upon how widely one will look in the duration–frequency domain. The non-stationarity of the signal might be seen as a problem in allowing long object durations ( $>0.25 \text{ s}$ ) since the objects have been assumed to have a fairly constant frequency over time (defined by mean frequency) and the signal does not have that property. But the signal is able to vary rapidly even while objects do not, either through overlapping objects, or activity at other frequencies, and, of course, the signal does not always change rapidly. Allowing durations of  $0.5$ – $10 \text{ s}$  and frequencies of  $2$ – $10 \text{ Hz}$ , we obtained 405 objects in total from the 50 data sets. Note that this range of values particularly excludes a large cluster of low-frequency objects. Mixture distribution analysis of the identified object characteristics derived from the 50 data sets gave rise to three distributions (as shown in Fig. 5). The distributions had mean frequen-



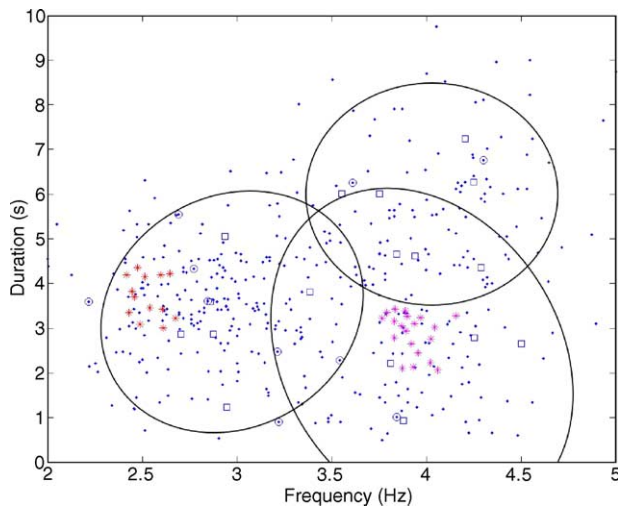


Fig. 5. Mixture distributions for object characteristics in the duration–frequency domain. Analysis of the 50 extracellular field recording data sets gave rise to approximately 830 identified objects over the entire time–frequency domain. Of these objects, 405 sit within the ranges shown and their characteristics are displayed as filled blue circles in the duration–frequency plot within. EM algorithm fit to the 405 identified object characteristics produces three normal distributions. Curves are drawn at 2 standard deviations of these distributions. Depending upon initial values chosen, distribution shape varied as well as proportions, but there was stability for the mean of frequency and durations within the range of frequencies and durations used. They are:  $2.9 \pm 0.2$ ,  $4.0 \pm 0.3$ ,  $4.1 \pm 0.2$  Hz for mean frequencies, and  $4 \pm 1$ ,  $3 \pm 1$ ,  $6 \pm 1$  s for the corresponding durations. Characteristics of objects identified from a single field data set are shown with blue unfilled circles (encircling blue filled circles). There were 10 objects identified from this particular data set, and their characteristics are not clustered in any particular distribution. The unfilled blue squares represent characteristics of objects identified from an additional field recording. There were 17 objects identified from this additional data set, and again their characteristics are not clustered in any particular distribution. However, it is clear that the identified object characteristics do lie within the fitted distributions. Red and purple stars are identified object characteristics from two separate intracellular recording data sets. Note that in this case the identified object characteristics from each data set are clustered in particular distributions.

cies and durations of (2.9 Hz, 4 s; 4.0 Hz, 3 s; 4.1 Hz, 6 s) and weightings of approximately (0.4, 0.3, 0.3), respectively. In Fig. 5, curves are drawn at 2 standard deviations of these distributions. Two distributions fit would generally yield a low frequency (3 Hz) and a higher frequency (4 Hz) component, but the fit generated numerous outliers. Four distributions fit would frequently result in the loss of one distribution through application of the algorithm; either by very low weighting, or convergence to parameters similar to another distribution. A qualitative feature of the duration–frequency plot which does suggest the suitability of the three distributions is the presence of three “corners” that are visible when looking at the perimeter of the high density distribution of points. Although this is not visually clear, the density of the distributions were also very well fit. Expanding the range of durations explored produced more objects and more clusters, particularly in the low duration range. Resolution and non-stationarity became limiting factors at that point. Expanding the range of frequen-

cies did not produce many more objects in the low frequency range (due to homogeneity, not low power), and while objects do appear in higher frequencies, they contribute less to the signal.

We treated the variation in parameter estimates with respect to different initial conditions choices as our error. Errors were large in the values obtained for weightings and covariance matrices, but there was reasonable stability in the mean frequency and durations obtained, as seen in Fig. 5. The overall quality of the fit was very good and was significantly better than the fit with two distributions with  $p < 0.01$ . To illustrate the distribution of object characteristics we show the characteristics of identified objects from one of the 50 distributions (see open circles in Fig. 5). Note that these circles are not clustered in any one of the three mixture distributions. We also identified objects from a single additional field recording and the characteristics of these identified objects are shown as open squares in Fig. 5. Again, note that they are not clustered in any of the particular distributions. Moreover, it is clear that the characteristics of these additional objects are captured by the three distributions produced by our method using the 50 extracellular data sets. On the data generated from noise, the objects obtained produced at most a unimodal distribution.

### 3.4. Intracellular data

We then examined some intracellular recordings obtained during the extracellular field recordings. In light of the three mixture distributions produced from the 50 data sets, we thought that it would be interesting to see what they might produce. An example of the raw intracellular recording is shown in Fig. 6A. The intracellular recordings, while clearly different from field recordings (Fig. 2A) in their raw signal (Fig. 6A) exhibited similar patterns in the time–frequency domain (Fig. 6B). We applied the same analyses as in the field data to two sets of intracellular recordings and obtained some notable differences. That is, we used the same time–frequency transformation (STFT) and computed our object perimeters using the same technique, with objects characterized in the same way. Because the methodology is, in part, being tested against the intracellular data, we did not redesign the methodology to suit the data. Because the methodology is quite general, this is less likely to be problematic in obtaining results and even the presence of spikes did not change the qualitative features of the data (different timescale).

The exhibited time–frequency highs in power were much less variable in their duration and frequency than the data from individual field recordings. These local highs accounted for a lower proportion of the signal output and were also less regular in shape and distinct in boundary relative to extracellular data. In Fig. 5, the intracellular data is shown as colored stars, a different color for each of the two intracellular data sets. It can be seen that characteristics of the identified objects are more tightly clustered than the extracellular

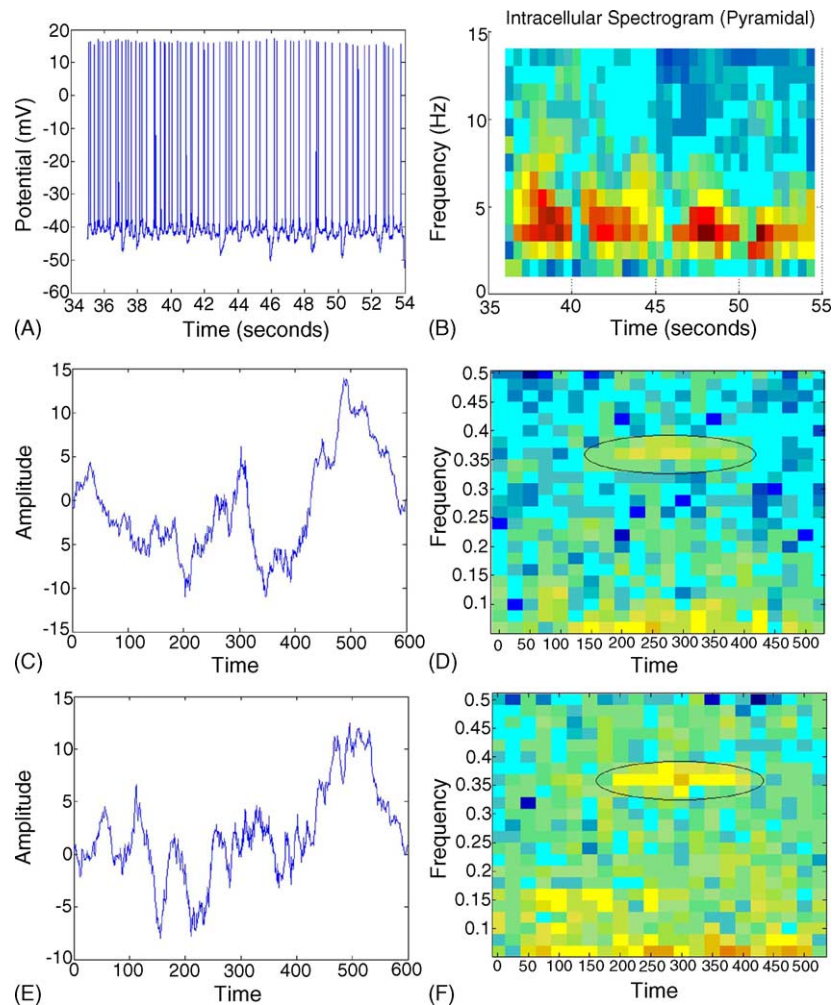


Fig. 6. Signals and their time–frequency transforms. Top: intracellular recording and its Spectrogram. (A) Example of a 20 s intracellular recording from a pyramidal cell in the intact hippocampal preparation. (B) Coarse-grain Spectrogram of the 20 s signal shown in (A). Same color scheme as in Fig. 3. Middle and bottom: on the left side ((C) and (E)) are shown two differing signals generated with some underlying similarities in general trends, but not at fine scales or in phase relationship. On the right side ((D) and (F)) are  $T$ – $F$  representations generated using the Gabor transform. The spectrograms show a clear similarity in behaviour with respect to power in that domain. Arbitrary scale and axis units. Same color scheme as in Fig. 3.

data, with durations and mean frequencies of  $(3.6 \pm 0.1$  s,  $2.7 \pm 0.1$  Hz) and  $(3.2 \pm 0.1$  s,  $3.9 \pm 0.1$  Hz) for the two data sets. However, individual objects were less well defined in the time–frequency domain in the case of intracellular data—less regular shapes and less well-defined edges. In other words, time–frequency characteristics were more consistent, but power characteristics were less consistent. It should be noted that the two intracellular recordings also differed substantially from one another, forming clusters in the characterized distributions.

#### 4. Discussion

In the time–frequency domain, a signal recording constitutes a distribution of frequencies that are changing with time—a non-stationary rhythm. A classification of those dis-

tributions offers a way of reducing signal behaviour into separable components drawn from the distribution of frequencies it exhibits over time. By way of analogy, this methodology resembles spike-sorting, with three central aspects: (1) representation of key features in an appropriate domain (time–frequency); (2) feature extraction in that domain; and (3) feature classification by clustering or mixture distribution. For example, in Buzsáki et al. (2003) the three sorting steps are respectively, filtering (frequency cutoff), power cutoff, and clustering (grouping cutoff). Spike sorting can also be determined from the intrinsic character of the signal (e.g., Letelier and Weber, 2000; Snider and Bonds, 1988). In this study, we developed a characterization of the signal by examining the time–frequency domain, characterizing local maxima by their time (duration) and frequency (mean frequency) parameters, and then grouping those parameters using the expectation–maximization (EM) algorithm. Together, our ap-

proach presents a natural and quantifiable way to characterize population rhythmic data. Through analysis of simultaneous intracellular data over the course of the 3 min recordings, we see that the methodology organizes signal characteristics in a manner suggestive of physiological organization. Object characteristics obtained from analysis of the intracellular data fell into only one of the distributions, unlike the object characteristics obtained from the field data sets which were present across all three component distributions. This presents the possibility that our approach may also be used to obtain the critical neuronal contributors of the population rhythm.

The hippocampal extracellular recordings collected from the mouse hippocampal isolate *in vitro* are non-stationary and exhibit a broad range of frequencies. In this work, we examined four popular specific methods of time–frequency analysis: The short time Fourier transform (STFT); the Wigner distribution; the exponential distribution; and the wavelet transform. We found the STFT best balanced competing demands for reasonable resolution without interference (as a STFT) and without excessive computation. In the STFT representation of the data, there were numerous distinct peaks, which frequently dominated the activity of the signal. Interestingly, the appearance of peaks rising above the surface defined by the STFT was qualitatively similar to the valleys falling below at intermediate values. Because these objects in the time–frequency domain exhibit high power and are distinct in their neighbourhood, they provide a way of characterizing the activity of the signal. In order to find patterns in this characterization, we plotted the duration and frequency of the objects obtained through our detection procedure. Cluster analysis offers a technique for separating data into more homogeneous subgroupings. A variation on this is finite mixture distribution analysis, which estimates the parameters defining statistical populations and can be used to interpret data in terms of the action of these populations. Using the EM algorithm we interpreted our complete collection of data in terms of three populations in the duration–frequency domain.

Because this analysis is performed in terms of the distribution of the time–frequency features of the hippocampal rhythm, it serves to measure the diversity of that signal behaviour in the time–frequency domain. Further, because it is believed that the SRFs of the intact hippocampus are dependent on interneuron coherence (Wu et al., 2002), the development of methods for studying its signal time–frequency diversity may be considered as a way to understand the diversity of interneuron characteristics that are known to be expressed (McBain and Fisahn, 2001, and see also Wilson and McNaughton, 1993, for functional relevance of ensemble characteristics). In particular, we showed that individual intracellular recordings give rise to a subset of the population (extracellular) recordings in the time–frequency domain. Thus, this method may also be useful in determining the extent to which different cells might contribute to population rhythms. Together with

present techniques of examining simultaneous phase relationships (which are limited), our method offers a powerful approach for obtaining neuronal and network constraints and thus of possible mechanisms that give rise to population rhythms.

The SRFs recorded in the intact hippocampus have frequencies that can be considered theta-like (3–12 Hz). The theta rhythm is thought to be important for coding in neuronal ensembles as well as the alteration of synaptic weights (Buzsáki, 2002). An early model of theta activity holds that medial septum-diagonal band of Broca (MS-DBB) neurons are pacemaker neurons for the theta rhythm (Bland and Colom, 1993). Distinct inhibitory and excitatory inputs to pyramidal cells are thought to generate the distinctive amplitude/phase versus depth pattern of theta oscillation through the interaction of the two current generators (Buzsáki, 2002). Some deficiencies in this model are based around the timing of inhibitory and excitatory inputs, functional considerations and further studies on patterns of activity, such as intrinsic theta behaviour in pyramidal neurons, and connectivity (e.g., Buzsáki et al., 1986; Buzsáki, 2002; O'Keefe and Recce, 1993). Although the rhythm in these field recordings sits largely within the theta range of 3–12 Hz, it is unclear that it falls into the category of the theta rhythms seen *in vivo*. Furthermore, oscillations in the higher end of theta range in association with more complex patterns can be generated in hippocampal slices (e.g., Bland et al., 1988; Fellous and Sejnowski, 2000) and in the whole hippocampal preparation (Wu et al., 2002), by the addition of carbachol. Because the mechanism whereby theta rhythms arise *in vitro* remains unclear, the methodology developed could be relevant to relating rhythms to intracellular properties such as intrinsic theta susceptibility.

Let us now consider that the three distributions identified from the field data describe the spontaneous rhythm expressed by the hippocampal isolate. Note that these distributions come from the pooled experimental data, and would not arise from the analysis of any one experiment. Looking at the distribution of object characteristics from one recording (squares in Fig. 5) we can see that they overlap each of the three distributions. However, the intracellular data also shown (stars) exhibits much less variability in the feature space, and can sit easily within a single distribution. So, the distributions arising from the intracellular recordings did not coincide with those generated from the field data. Their separate but comparatively simple distributions suggest that the distribution of field rhythms may be reflective of neuronal characteristics or diversity. These related patterns of activity are unlikely to be discernable using typical analysis techniques, such as phase relationships and correlations. This is illustrated in Fig. 6. Fig. 6 shows two artificial signals on the left (C, E) which were generated to contain an interesting similarity in the time–frequency domain (Fig. 6D and F). This similarity would not be uncovered by an examination of their spiking dynamics without a very particular filtering

(biasing). The identified patterns of activity certainly suggest this as an avenue for future study, and as in Fig. 6 (middle and bottom), this methodology will be helpful in making such a comparison.

Epilepsy is an area of relevance for these techniques. Characterization and feature extraction of relevant EEG signals has been performed using the Gabor and Wavelet transforms (Hazarika et al., 1997; Quiroga et al., 1997; Schiff et al., 2000; Shen et al., 2001). Even simple signal properties such as power have been found to play an important and potentially predictive role in the occurrence of epileptic seizures (Litt et al., 2001). The techniques developed here could be applied to epilepsy EEG data. This technique may also have relevance to auditory research, where time–frequency analysis has been similarly used to suggest functional groupings or associations (e.g., Miller et al., 2001).

#### 4.1. Summary

The complex appearance of the signal from the intact hippocampus represents heterogeneities in the frequency distribution as a function of time. Using the combined techniques of time–frequency analysis, followed by object identification, and cluster analysis, we have deconstructed the signal heterogeneities into possible simple components. These components provide a characterization of the hippocampal rhythm into different classes of activity based solely on the signal properties themselves. Further, these components may have physiological significance. In particular, the rhythmic activity of the hippocampal preparation is thought by Wu et al. to have its genesis in the synchronous activity of interneurons, whose characteristics within the hippocampus are known to be highly diverse. Using the method described in this paper, we have reduced the signal to the activity of distinct statistical populations, and because (a) these spatio-temporal features are believed to result from networked interneurons, (b) these interneurons are believed to have developed their diverse characteristics in order to produce distinct temporal and frequency behaviours, and (c) intracellular (pyramidal) recordings do not exhibit this diversity, we suggest that the diversity or variability in the distribution of time–frequency features in the intact hippocampus can be related to the diversity of interneurons. It remains to be explored with sufficient intracellular data whether the time–frequency characteristics of field data can be definitively attributed to intracellular behaviour in the way our data and method suggests.

#### Acknowledgments

We thank H. Shen for sharing intracellular data. This work was supported by grants from NSERC (FKS) and CIHR (LZ). FKS is an MRC (CIHR) Scholar and a CFI Researcher. JAG was supported by Canada Graduate Scholarship (CGS) and NSERC student awards.

## Appendix A

### A.1. T–F analyses

The usual approach to dealing with non-stationary rhythms is to divide them into stationary pieces. Two general ways of accomplishing this are the Cohen transform and the Wavelet transform. The Cohen transform is defined by

$$C(t, \omega, \phi) = \int \int \int \exp(i(-\theta t - \tau\theta + \omega u)) \phi(\theta, \tau) x \times \left(u + \frac{\tau}{2}\right) x^* \left(u - \frac{\tau}{2}\right) du d\tau d\theta$$

$x(t)$  is the signal,  $\omega$  the frequency,  $x^*(t)$  the complex conjugate, and  $\phi(\theta, \tau)$  is the kernel and divides the time–frequency domain into tiles of equal size for a given transform (Cohen, 1989). The most common example is the STFT:

$$\text{STFT}(t, \omega) = \int x(\tau) h(\tau - t) \exp(-i\omega\tau) d\tau$$

where  $h(t)$  is the window function. A rectangular window gives high overall resolution but induces Gibbs ripple, so a smooth window choice is necessary to improve frequency resolution. Beyond that, with increasing frequency resolution comes proportionately decreasing frequency resolution according to the uncertainty principle, and the product of resolutions has a lower bound for a given transform. Determining the optimal window for a signal depends on the qualitative features of interest as well as the degree of non-stationarity (for examples, see Akay, 1998 and Schiff et al., 2000). We compared the (non-normal) mean frequency data for consecutive bins using the Kruskal–Wallis, testing that the mean for the frequency distributions was not significantly changed at our chosen resolution. The usual representation of time–frequency STFT data is in the form of the spectrogram, or STFT magnitude squared. These methods can be thought of as bandpass filters performed over a range of frequencies. To improve on the STFT, the Wigner distribution is frequently used, defined by

$$\text{Wigner}(t, \omega) = \int x\left(t + \frac{\tau}{2}\right) x^*\left(t - \frac{\tau}{2}\right) \exp(-i\omega\tau) d\tau$$

That is, it is a transform from Cohen's class with a kernel of 1 (Claassen and Mecklenbrauker, 1980; Wigner, 1932). While this offers improved resolution, if the signal  $x(t) = a(t) + b(t)$  then the magnitude of the Wigner distribution will take the form  $W_{aa}(t, \omega) + W_{ab}(t, \omega) + W_{ba}(t, \omega) + W_{bb}(t, \omega)$ , where the middle two terms are cross-terms that generate an artifact—time–frequency activity where the signal is inactive.

A third of Cohen's class of distribution is the Choi–Williams or exponential distribution which we also considered for our data of extracellular EEG recordings. In the case of the exponential distribution, the kernel takes the form  $\phi(\theta, \tau) = \exp(-\theta^2 \tau^2 / \sigma)$  where the distribution param-



eter  $\sigma$  allows one to shift from a Wigner-like transform for high  $\sigma$  to a more STFT-like transform for low  $\sigma$  (Choi and Williams, 1989). In our case, the distribution parameter was set to 0.5, 1 and 10 and the data examined for particular suitability or features of interest. Over the range of parameter values chosen, the exponential distribution shifted in appearance from STFT-like to Wigner—the differences were mostly minor between the STFT and exponential, and Wigner and exponential in those cases with some common deficits in performance (Baraniuk and Jones, 1993).

A popular alternative to these methods which divide the time–frequency domain into equal pieces is the wavelet transform which divides the time–frequency domain into different sized pieces depending on frequency. For high frequency, the time resolution is good and the frequency resolution bad, and vice versa for low-frequency—an intuitive property. The wavelet transform is defined by:

$$\text{wavelet}(t, a) = \frac{1}{\sqrt{a}} \int x(\tau) h^* \frac{\tau - t}{a} d\tau$$

where  $h^*(t)$  is the analyzing wavelet, and  $a$  is the scale—the scalogram is obtained by taking the squared magnitude of the transform. A wavelet can be described as a finite energy burst in the time domain with oscillation in time (Combes et al., 1989). The wavelet used to examine our data was the Haar wavelet which takes the value 1 on  $(-1/2, 0]$  and  $-1$  on  $(0, 1/2]$  and zero elsewhere in its domain—with bandwidths proportional to frequency, differences at multiple scales (Teolis, 1998). While techniques do exist (signal replication, specific constraints) for choosing the wavelet to be especially appropriate to the signal, this is also typically a qualitative choice. The Haar wavelet is computationally simple, and also has some similarities to our later edge detection. The wavelet transform was specifically examined to determine whether gradient based features or object identification were directly possible from the signal before any other transformation. In the case of the Haar wavelet transform applied to our data, the very small scale coefficients resulting from this transform correspond to shape parameters for the peaks and exhibited no strong trends in distribution that would allow peak/spike sorting; there was no clear multimodality within any of the parameter distributions in this range. The medium scale parameters exhibited the same qualitative properties as in the case of the Cohen distributions. The special property of the wavelet transform, its changing resolution with frequency was not particularly advantageous over the range of values seen.

## A.2. Object identification analyses

Edges occur where the data is rapidly changing in the  $z$ -axis, and we determine the precise placement of the perimeter by calculating the second derivative of intensity,  $D^2(\text{Spectrogram}) = 0$  calculated in the appropriate direction, which is defined by the orientation formed by zero crossings. In smoothed or smooth images, such as ours, the con-

dition of linear variation near zero crossings hold, and the direction may be found by the Laplacian (Marr and Hildreth, 1980). Our data was not smoothed beyond that set by the resolution—e.g., smoothed at the  $T$ – $F$  resolution of the data.

## A.3. Feature mixture distribution analyses

For  $k$  clusters, a mixture density  $f(\vec{y})$  has the form:

$$f(\vec{y}) = \sum_{j=1}^k p_j f_j(\vec{y})$$

with  $p_j$  being the weighting coefficient and  $f_j$  representing the component density for the  $j$ th distribution with random variables  $\vec{y}$ .

Let  $\vec{X} = (X_1, \dots, X_k)^T$  represent a multinomial random vector with exactly one  $X_j$  equal to 1 and the others zero, with  $p_j = \Pr[X_j = 1]$ ,  $j = 1, \dots, k$  and where each  $p_j > 0$  and all  $p_j$ 's for  $k = 1, \dots, k$  sums to one. The pdf of  $\vec{X}$  is  $f_x(x_1, \dots, x_k) = \prod_{j=1}^k p_j^{x_j}$ .

Now, let  $\vec{Y} = (Y_1, \dots, Y_m)^T$  represent a random variable defined conditionally on  $\vec{X}$ . Then the marginal density on  $\vec{Y}$  is  $f_y(\vec{y}) = \sum \prod_{j=1}^k [p_j f_j(\vec{y})]^{x_j} = \sum_{j=1}^k p_j f_j(\vec{y})$ , that is, a finite mixture distribution. We define the posterior probabilities,  $p_{jy}$  as

$$p_{jy} = \Pr[X_j = 1 | \vec{Y} = \vec{y}] = \frac{p_j f_j(\vec{y})}{\sum_{h=1}^k p_h f_h(\vec{y})}$$

$$j = 1, \dots, k$$

Consider the sample

$$\begin{pmatrix} \vec{X}_1 \\ \vec{Y}_1 \end{pmatrix}, \dots, \begin{pmatrix} \vec{X}_N \\ \vec{Y}_N \end{pmatrix}$$

from the joint distribution of  $\vec{X}$  and  $\vec{Y}$ . We take

$$\vec{X}_i = \begin{pmatrix} X_{1i} \\ \dots \\ X_{ki} \end{pmatrix}$$

as the  $i$ th observation for the vector of variables. Then the complete log-likelihood function,  $l_c$  for the unknown parameters, and  $N \vec{X}_i$  and  $\vec{Y}_i$  becomes

$$l_c = \sum_{i=1}^N \sum_{j=1}^k x_{ji} \log[p_j f_j(\vec{y}_i)]$$

$$= \sum_{j=1}^k \sum_{x_{ji}=1} \log p_j + \sum_{j=1}^k \sum_{x_{ji}=1} \log f_j(\vec{y}_i)$$

The two halves of the likelihood equation can thus be maximized separately and after some calculation the iterative steps

of the EM algorithm for normal mixtures can be obtained:

$$\text{E-step: } \pi_{hi} = \frac{p_h f_h(\vec{y}_i)}{f(\vec{y}_i)}, \quad h = 1, \dots, k; \quad i = 1, \dots, N$$

$$\text{M-step: } p_h = \frac{1}{N} \sum_{i=1}^N p_{hi}, \quad h = 1, \dots, k,$$

$$\vec{\mu}_h = \frac{1}{N p_h} \sum_{i=1}^N p_{hi} \vec{y}_i, \quad h = 1, \dots, k,$$

$$\psi_h = \frac{1}{N p_h} \sum_{i=1}^N p_{hi} (\vec{y}_i - \vec{\mu}_h)(\vec{y}_i - \vec{\mu}_h)^T, \quad h = 1, \dots, k$$

where  $\vec{\mu}$  is the mean, and  $\psi$  the covariance matrix (Flury, 1997; Redner et al., 1984).

## References

- Achermann P, Borbély AA. Coherence analysis of the human sleep electroencephalogram. *Neuroscience* 1998;85:1195–208.
- Adeli H, Zhou Z, Dadmehr N. Analysis of EEG records in an epileptic patient using wavelet transform. *J Neurosci Meth* 2003;123:69–87.
- Andersen P, Soleng AF, Raastad M. The hippocampal lamella hypothesis revisited. *Brain Res* 2000;886:165–71.
- Akay M, editor. Time–frequency and wavelets in biomedical signal processing. New York: IEEE, Inc.; 1998.
- Baraniuk RG, Jones DJ. Signal-dependent time–frequency representation: optimal kernel design. *IEEE Trans Signal Process* 1993;41:1589–602.
- Bland BH, Colom LV. Extrinsic and intrinsic properties underlying oscillation and synchrony in limbic cortex. *Prog Neurobiol* 1993;41:157–208.
- Bland BH, Colom LV, Konopacki J, Roth SH. Intracellular records of carbachol-induced theta rhythm in hippocampal slices. *Brain Res* 1988;447:364–8.
- Buzsáki G. Theta oscillations in the hippocampus. *Neuron* 2002;33:325–40.
- Buzsáki G, Buhl DL, Harris KD, Csicsvari J, Czib B, Morozov A. Hippocampal network patterns of activity in the mouse. *Neuroscience* 2003;116:201–11.
- Buzsáki G, Czopf J, Kondakor I, Kellenyi L. Laminar distribution of hippocampal rhythmic slow activity (RSA) in the behaving rat: current source density analysis, effects of urethane and atropine. *Brain Res* 1986;365:125–37.
- Choi HI, Williams WJ. Improved time–frequency representation of multicomponent signals using exponential kernels. *IEEE Trans Acoust Speech Signal Process* 1989;6:862–71, ASSP-37.
- Claassen TCM, Mecklenbrauker WGF. The Wigner distribution—a tool for time–frequency signal analysis. *Philips J Res* 1980;35(276–300):217–50.
- Cohen L. Time–frequency distributions—a review. *Proc IEEE* 1989;77:941–81.
- Combes JM, Grossman A, Tchamitchian. Wavelets, time–frequency methods and phase space. Berlin: Springer; 1989.
- Csicsvari J, Hirase H, Mamiya A, Buzsáki G. Ensemble patterns of hippocampal CA3–CA1 neurons during sharp wave-associated population events. *Neuron* 2000;28:585–94.
- Dempster AP, Laird NM, Rubin DB. Maximum likelihood from incomplete data via the EM algorithm. *J R Statist Soc B* 1977;39:1–38.
- Everitt BS, Bullmore ET. Mixture model mapping of brain activation in functional magnetic resonance images. *Hum Brain Mapp* 1999;7:1–14.
- Everitt BS, Hand DJ. Finite mixture distributions. London: Chapman & Hall; 1981.
- Fellous JM, Sejnowski T. Cholinergic induction of oscillations in the hippocampal slice in the slow (0.5–2 Hz), theta (5–12 Hz) and gamma (35–70 Hz) bands. *Hippocampus* 2000;10:187–97.
- Flury B. A first course in multivariate statistics. New York: Springer; 1997.
- Gray CM, König P, Engel AK, Singer W. Oscillatory responses in cat visual cortex exhibit inter-columnar synchronization which reflects global stimulus properties. *Nature* 1989;338:334–7.
- Hampson RE, Simeral JD, Deadwyler SA. Distribution of spatial and non-spatial information in dorsal hippocampus. *Nature* 1999;402:610–4.
- Hazarika N, Chen J, Tsoi A, Sergejew A. Classification of EEG signals using the wavelet transform. *Signal Process* 1997;59:61–72.
- Huerta PT, Lisman JE. Heightened synaptic plasticity of hippocampal CA1 neurons during a cholinergically induced rhythmic state. *Nature* 1993;364:723–5.
- Johnston D, Amaral D. Hippocampus. In: Shepherd GM, editor. The synaptic organization of the brain. New York: Oxford University Press; 1998. p. 417–58.
- Kadambe S, Boudreaux-Bartels GF. A comparison of the existence of “cross terms” in the Wigner distribution and the squared magnitude of the wavelet transform and the short time Fourier transform. *IEEE Trans Signal Process* 1992;40:2498–517.
- Kudrimoti HS, Barnes CA, MacNaughton BL. Reactivation of hippocampal cell assemblies: effects of behavioral state, experience, and EEG dynamics. *J Neurosci* 1999;19:4090–101.
- Letelier JC, Weber P. Spike sorting based on discrete wavelet transform coefficients. *J Neurosci Meth* 2000;101:93–106.
- Li XG, Somogyi P, Ylinen A, Buzsáki G. The hippocampal CA3 network: an in vivo intracellular labeling study. *J Comp Neurol* 1994;339:181–208.
- Litt B, Esteller R, Echaz J, D’Alessandro M, Shor R, Henry T, et al. Epileptic seizures may begin hours in advance of clinical onset: a report of five patients. *Neuron* 2001;30:51–64.
- Marr D, Hildreth E. Theory of edge detection. *Proc R Soc London B* 1980;207:187–217.
- McBain CJ, Fisahn A. Interneurons unbound. *Nat Rev Neurosci* 2001;2:11–23.
- McLachlan. On bootstrapping the likelihood ratio test statistic for the number of components in a normal mixture. *Appl Statist* 1987;37:318–24.
- Miller LM, Escabi MA, Read HL, Schreiner CE. Functional convergence of response properties in the auditory thalamocortical system. *Neuron* 2001;32:151–60.
- Morrone MC, Owens RA. Feature detection from local energy. *Pattern Recogn Lett* 1987;6:303–13.
- Moser MB, Moser EI. Distributed encoding and retrieval of spatial memory in the hippocampus. *J Neurosci* 1998;18:7535–42.
- Nicolelis MA, Baccala LA, Lin RCS, Chapin JK. Sensorimotor encoding by synchronous neural ensemble activity at multiple levels of the somatosensory system. *Science* 1995;268:1353–8.
- Nicolelis MA, Ribeiro S. Multielectrode recordings: the next steps. *Curr Opin Neurobiol* 2002;12(5):602–6.
- Oddie SD, Bland BH. Hippocampal formation theta activity and movement selection. *Neurosci Biobehav Rev* 1998;22:221–31.
- O’Keefe J, Recce ML. Phase relationship between hippocampal place units and the EEG theta rhythm. *Hippocampus* 1993;3:317–30.
- Ponomarev AL, Davis RL. An adjustable-threshold algorithm for the identification of objects in three-dimensional images. *Bioinformatics* 2003;19:1431–5.
- Quiñ Quiroga R, Blano S, Rosso O, García H, Rabinowicz A. Searching for hidden information with Gabor transform in generalized tonic-clonic seizures. *Electroen Clin Neuro* 1997;103:434–9.
- Redner RA, Walker HF. Mixture densities, maximum likelihood, and the EM algorithm. *SIAM Rev* 1984;26(2):195–239.

- Refinetti R. Non-stationary time series and the robustness of circadian rhythms. *J Theor Biol* 2004;227:571–81.
- Rieke F, Bialek W, Warland D. *Spikes: exploring the neural code*. Boston: MIT Press; 1997.
- Schiff SJ, Colella D, Jacyna GM, Hughes E, Creekmore JW, Marshall A, et al. Brain chirps: spectrographic signatures of epileptic seizures. *Clin Neurophys* 2000;111(6):953–8.
- Shen M, Sun L, Chan F. Method for extracting time-varying rhythms of electroencephalography via wavelet packet analysis. *IEEE Proc Meas Technol* 2001;148:23–7.
- Sirota A, Csicsvari J, Buhl D, Buzsáki G. Communication between neocortex and hippocampus during sleep in rodents. *Proc Natl Acad Sci* 2003;100(4):2065–9.
- Snider RK, Bonds AB. Classification of non-stationary neural signals. *J Neurosci Meth* 1988;84:155–66.
- Teolis A. *Computational signal processing with wavelets*. Boston: Birkhauser; 1998.
- Tomazic S. On short-time Fourier transform with single sided exponential window. *Signal Process* 1996;55:141–8.
- Vanderwolf CH. Hippocampal electrical activity and voluntary movement in the rat. *Electroen Clin Neurol* 1969;26:407–18.
- Wigner E. On the quantum correction for thermodynamic equilibrium. *Phys Rev* 1932;40:749–59.
- Wilson MA, McNaughton BL. Dynamics of the hippocampal ensemble code for space. *Science* 1993;261:1055–8.
- Wolfe JH. Pattern clustering by multivariate mixture analysis. *Multivar Behav Res* 1970;5:329–50.
- Wu C, Shen H, Luk WP, Zhang L. A fundamental oscillatory state of isolated rodent hippocampus. *J Physiol* 2002;540(2):509–27.